Catalysis Science & Technology

ROYAL SOCIETY OF CHEMISTRY

PAPER

View Article Online
View Journal | View Issue

Cite this: *Catal. Sci. Technol.*, 2025, **15**, 2034

Toward decorrelation of surface oxygen groups from metal dispersion effects in Pd/C hydrogenation catalysts†

Edgardo A. Leal Villarroel,[ab] Cécile Marcelot,[c] Cecilia C. Torres,[d] Katerina Soulantica,[e] Cristian H. Campos *[bd] and Philippe Serp *[af]

Received 29th December 2024,
Accepted 4th February 2025

DOI: 10.1039/d4cy01562b

rsc.li/catalysis

Carbon-supported Pd-based catalysts have found wide applications in hydrogenation of specific functional groups. Surface modification of the support, *via* the introduction of oxygen functional groups, modulates the metal dispersion and the interaction of reactant(s) with the catalyst surface, consequently tuning its catalytic properties. However, it is difficult to decorrelate the effect of surface oxygen groups from that of the dispersion of the metallic phase. This study aims at decorrelating these effects on the catalytic performance for phenylacetylene hydrogenation by using preformed monodispersed Pd nanoparticles deposited on carbon supports presenting different densities of surface oxygen groups. X-ray photoelectron spectroscopy, temperature-programmed decomposition experiments and transmission electron microscopy were used to analyze the dispersion and oxidation state of Pd and the concentration of surface oxygen groups. The results reveal that such decorrelation is not an easy task, particularly since spillover of the nanoparticles' native capping ligand (oleylamine) occurs during Pd particle deposition. This phenomenon, which depends on the density of oxygen functional groups and the size of Pd particles, impacts the $Pd^{(0)}/Pd^{2+}$ ratio and the surface Pd/N atomic ratio. These two last parameters, which seem to be interconnected, significantly impact the catalytic performance.

Introduction

In supported metal catalysts, which catalyze many major industrial chemical reactions, the nature of both the active phase and the support can influence the catalytic performance.[1] The support plays an important role not only by positioning itself as a macromolecular ligand, as its surface chemistry can contribute directly or indirectly to the reactivity, but also by conditioning the nature of the active site(s).[2,3] In the case of carbon-supported catalysts, oxygen-containing functional groups (OFGs) are the most common functionalities present on the carbon surface, and among the different carbon surface modification methods, carbon surface oxidation is the most popular.[4,5] The effects of OFGs of carbon supports on catalysis have been discussed.[6] The OGFs can (i) play a crucial role in the anchoring of the active phase, (ii) have a significant impact on charge transfer and hydrogen spillover, or (iii) either be involved in the adsorption/desorption steps or directly participate in the chemical transformation.

Supported Pd catalysts are very efficient hydrogenation catalysts because of the low activation energy for H_2 dissociative chemisorption on the palladium surface and the easy diffusion of hydrogen atoms into the bulk (formation of Pd hydride phases).[7] According to published data, up to 75% of hydrogenation reactions are carried out in the presence of Pd/C catalysts.[8] The possibility of regulating the catalytic properties of carbon-supported Pd catalysts by modulating the OFG concentration and type has been investigated in the past.[6,9] The introduction of significant quantities of OFGs by oxidizing the carbon support allows modulation of the hydrogenation activity of Pd nanoparticles (Pd_{NP}) through different and often intercorrelated effects. It generally leads to a better Pd dispersion,[10–17] but it can also induce electronic metal–support interaction (EMSI) effects[18] that impact the chemical states of the Pd species,[15,17] or facilitate hydrogen spillover.[19] All these effects can be operative during hydrogenation reactions.[17] In addition, the introduction of

[a] *LCC-CNRS, UPR 8241 CNRS, UPS, INPT, Université de Toulouse, 4 allée Emile Monso, 31030 Toulouse, France. E-mail: philippe.serp@ensiacet.fr*
[b] *Departamento de Físico-Química, Facultad de Ciencias Químicas, Universidad de Concepción, Edmundo Larenas 129, Casilla 160-C, Concepción, Chile*
[c] *CEMES, UPR 8011 CNRS, Université de Toulouse, 29 Rue Jeanne Marvig, 31400 Toulouse, France*
[d] *Departamento de Ciencias Químicas, Facultad de Ciencias Exactas, Universidad Andres Bello, Autopista Concepción-Talcahuano 7100, Talcahuano 4300866, Chile. E-mail: cristian.campos.f@unab.cl*
[e] *LPCNO, CNRS, INSA, UPS UMR 5215, Université de Toulouse, 31077 Toulouse, France*
[f] *Institut universitaire de France (IUF), France*

† Electronic supplementary information (ESI) available. See DOI: https://doi.org/10.1039/d4cy01562b

OFGs increases the hydrophilicity of the carbon surface, which can positively impact the adsorption/activation of polar reactant molecules, impairing on the other hand those of apolar reactants.[20,21]

One possibility to decorrelate these effects, and in particular those related to the active phase (dispersion, oxidation state) and the support (adsorption, spillover), would be to use preformed monodispersed Pd nanoparticles ($Pd_{p\text{-}NP}$) produced through colloidal synthesis methods. To the best of our knowledge, very few efforts have been devoted to go in that direction. One can cite the work of Prati *et al.*, who used polyvinyl alcohol protected $Pd_{p\text{-}NP}$ deposited on graphene nanoplatelets for benzaldehyde hydrogenation.[22] In this work, the authors have shown that for 3.5–3.9 nm $Pd_{p\text{-}NP}$, increasing the concentration of OFGs resulted in a decrease in catalytic activity. The presence of OFGs not only induces a weaker interaction between the carbonyl group of benzaldehyde and the surface of the support but also impacts the Pd^0/Pd^{2+} surface ratio. These parameters apparently act in opposite directions on catalyst activity. Therefore, further efforts are required to investigate these effects, particularly for non-polar organic substrates.

In this work, we use carbon nanotubes (CNTs) which have been oxidized with nitric acid to introduce various amounts of OFGs to immobilize $Pd_{p\text{-}NP}$ of different sizes mainly stabilized by oleylamine (OAm) ligands. The resulting catalysts have been characterized and tested for phenylacetylene (PhA) selective hydrogenation, a reaction for which carbon-supported Pd colloids have shown interesting performances with high selectivity toward styrene (ST).[23] Beside the effect of metal dispersion and OFGs, we also investigated the effects of (i) active site speciation by using Pd single atoms and Pd_{NP} and (ii) spatial gradients on catalyst performances.

Experimental

General methods

Oleylamine (OAm), oleic acid (OAc), palladium(II) acetylacetonate 99% [$Pd(acac)_2$] and palladium(II) nitrate hydrate ($Pd(NO_3)_2{\cdot}xH_2O$) were provided by Sigma Aldrich. Tetrabutylammonium bromide (TBAB) was provided by Across Organics and phenylacetylene (PhA) by Thermo Scientific. Tris(dibenzylideneacetone)dipalladium [$Pd_2(dba)_3$] was provided by Nanomeps (Toulouse, France). Ethanol, chloroform, pentane, *n*-hexane and all the solvents were provided by VWR Chemicals. According to the necessity, the solvents were purified and degassed prior to utilization.

The CNTs were produced, purified and oxidized according to a previously reported procedure.[13] The CNTs were synthesized by CVD in a fluidized bed reactor; ethylene (C_2H_4) was employed as a source of carbon and $AlFeCoO_4$ was used as a catalyst. Prior to synthesis the catalyst was reduced at 675 °C, then an ethylene flow through the reactor was established for 30 min. After the synthesis the CNTs were purified by heating them at 140 °C for 3 h in a mixture of sulfuric acid : water (50 : 50) to obtain CNT_P. The CNT_P were then chemically oxidized with nitric acid (65%) at 140 °C for 1, 3 and 5 h, after which the solids were washed with deionized water until a neutral pH was reached. The solids were then dried overnight at 80 °C to obtain CNT_1, CNT_3 and CNT_5, respectively.

Synthesis of $Pd_{p\text{-}NP}$

$Pd_{2.4}$ nanoparticles of 2.4 nm mean size were prepared according to the Sato group's report.[24] First, 118.6 mg (0.389 mmol) of [$Pd(acac)_2$] were mixed in a three-neck flask under an argon flow with 3.3 mL of OAm (10 mmol) to obtain a yellow homogeneous solution. Then, 3.2 mL of OAc (10.14 mmol) were added and the solution was stirred at 1000 rpm in order to ensure a homogeneous solution upon heating at 50 °C. Finally, a fresh solution of 387 mg (1.5 mmol) of TBAB in chloroform (2 mL) was added under stirring and the reaction was kept for 60 min at 50 °C. After that, the nanoparticles were washed three times with 30 mL of ethanol and stored in *n*-hexane.

$Pd_{4.4}$ nanoparticles of 4.4 nm mean size were prepared according to the Kılıç method.[25] 75.6 mg (0.248 mmol) of [$Pd(acac)_2$] in 12 mL (36.3 mmol) of OAm were mixed in a three-neck flask under an argon flow. The solution was slowly heated at 75 °C. When the solution reached 75 °C, a fresh solution of 355 mg (1.45 mmol) of TBAB and 32 mL (90.75 mmol) of OAm was introduced. Then, the solution was quickly heated at 95 °C and kept for 1 h under stirring at 1000 rpm. The obtained nanoparticles were washed three times with 30 mL of ethanol and redispersed in degassed *n*-hexane.

For both syntheses, a portion of the dispersion of the nanoparticles was dried and analyzed by ICP to know the percentage of palladium.

Preparation of carbon-supported Pd catalysts

The carbon-supported Pd catalysts were prepared on different CNT supports bearing different OFG amounts (CNT_P, CNT_1, CNT_3 and CNT_5). The Pd was introduced as (i) preformed Pd NPs ($Pd_{p\text{-}NP}$), (ii) NPs formed by impregnation with Pd nitrate (Pd_{NP}) and (iii) single atoms by coming in contact with $Pd_2(dba)_3$ (Pd_{SA}).

The $Pd_{2.4/4.4}/CNT_x$ catalysts were prepared by wet impregnation on CNT_P, CNT_1, CNT_3 and CNT_5. The CNT_x were first activated at 400 °C for 1 h under an argon flow. The required amount of $Pd_{p\text{-}NP}$ dispersed in degassed pentane to reach 1% (w/w) of Pd was added to a 40 mL pentane dispersion of CNTs. The solution was added to the CNT_x and kept under stirring overnight. After filtration and washing with 2 portions of 20 mL of pentane, the solid was dried at 120 °C and stored.

The Pd_{NP}/CNT_x catalysts were prepared by simple wet impregnation from Pd nitrate on CNT_1, CNT_3 and CNT_5.[26] The CNT_x were first activated at 400 °C for 1 h under an argon flow. The quantity of $Pd(NO_3)_2{\cdot}xH_2O$ necessary for a

1% (w/w) Pd loading was dissolved in 40 mL of degassed acetone. The activated CNTs (100 mg) were mixed with the palladium solution under argon and stirred overnight. After filtration and washing with acetone, the resulting solid was dried overnight at 120 °C and then reduced in a horizontal tube furnace under an 80% N_2/20% H_2 flow at 300 °C for 2 h.

The Pd_{SA}/CNT_5 catalyst containing mainly palladium single atoms (SAs) was prepared under a nitrogen atmosphere. The CNT_5 were first activated at 400 °C for 1 h under an argon flow. The required amount of $Pd_2(dba)_3$ to obtain 0.1% (w/w) loading was dissolved in 40 mL of purified toluene under a nitrogen atmosphere; the solution was added to the activated CNTs and kept under stirring overnight. Then, the solid was washed and dried at 120 °C for 24 h and was then reduced in a horizontal tube furnace under an 80% N_2/20% H_2 flow at 400 °C for 1 h.

Hydrogenation of phenylacetylene

The hydrogenation of PhA was carried out in a Top Industrie high-pressure and temperature stainless-steel autoclave equipped with a pressure and temperature controlling system. Typical experiments were carried out at 30 °C and 5 bar H_2. Before the reaction, the reactor was purged with 3 cycles of N_2/vacuum. The concentration of phenylacetylene was 0.082 mol L^{-1} using 30 mL of MeOH as solvent. The PhA : Pd molar ratio was 10 000. To follow the conversion of phenylacetylene and the selectivity to the desired products, gas chromatography (Perkin Elmer, Autosystem XL, Rtx-5amines column) was used, with *n*-decane as an internal standard.

To compare the different catalysts, the site time yield (STY) of the catalysts was calculated at full PhA conversion (STY_{100}) and corrected for the calculated dispersion of the catalysts to obtain the turnover frequency (TOF_{100}). The STY_{100} was calculated according to the following equation:

$$STY_{100} = \frac{n_{PhA}}{n_{Pd} \times t}$$

where n_{PhA} is the quantity (mol) of phenylacetylene, n_{Pd} is the quantity (mol) of Pd and t is the time (s) at which 100% convention of PhA was attained. The TOF_{100} was calculated taking into account the surface Pd atoms obtained from the calculated dispersion of the catalysts. Metal dispersion was evaluated from a universal mathematical relation between the mean relative size of metallic crystallites and their dispersion, as described elsewhere.[27]

Catalyst characterization

The palladium content of each catalyst was determined using inductively coupled plasma optical emission spectroscopy (ICP-OES). Elemental analyses for C, H and N were performed using a Perkin Elmer 2400 Series II elemental analyzer. TEM and HRTEM analyses were conducted at the Centre de Microcaracterisation Raimond Castaing, UMS 3623, Toulouse, using a MET JEOL JEM 1400 ORIUS instrument operating at 120 kV with a point resolution of 2.3 Å and a JEOL JEM-ARM200F Cold FEG system operating at 200 kV with a point resolution of <1.9 Å. The particle size distributions were determined by manually measuring enlarged micrographs from various areas of the TEM grid (with at least 300 particles). The samples were analyzed by X-ray photoelectron spectroscopy (XPS) using a VG Escalab MKII spectrometer with a non-monochromatized Mg K_α source (1253.6 eV). XRD patterns were recorded at room temperature using Cu K_α radiation (λ = 1.54 Å) and a parabolic MPD mirror for Cu radiation. Temperature-programmed decomposition (TPD-He) experiments were conducted using a 3Flex device (Micromeritics) coupled with a mass spectrometer (Cirrus 2, MKS Spectra product). Samples were pretreated under vacuum at 110 °C for 30 min followed by a He flow (60 mL min^{-1}) for another 30 min, and finally evacuated for 30 min at 35 °C before analysis. The samples were then heated at a rate of 10 °C min^{-1} up to 900 °C under a helium flow (100 mL min^{-1}) while recording the mass signals (m/z) for fragments 15, 18, 28, and 44 corresponding to CH_4, H_2O, CO, and CO_2, respectively. The CO and CO_2 MS signals were quantified by calibrating the detector using calcium oxalate as a standard.

Results and discussion

Carbon nanotube characterization

The purified CNTs (CNT_p) were oxidized in boiling nitric acid for 1, 3 and 5 h resulting in samples CNT_1, CNT_3 and CNT_5, respectively. Such a treatment is known to introduce various types of OFGs such as carbonyl, phenol and carboxylic groups.[28] The CNT_p (S_{BET} = 180 m^2 g^{-1}) are composed of agglomerates of 5–100 μm size, and the mean external diameter of CNTs is 15 nm. The nitric acid treatment results in some damage of the tube walls and contributes to the opening of CNT tips, as shown in Fig. S1† for sample CNT_3.[29] DFT calculations derived from N_2 adsorption data were used for the determination of basal plane, prismatic and defect surfaces of CNTs.[30] The absolute values and percentages of prismatic (edges), basal, and defect (surface steps or surface OFGs) surfaces of CNT_p and CNT_3 are given in Table S1† to illustrate the effect of the acidic treatment of these surfaces. Basically, HNO_3 oxidation increases the total surface area of the material. The surface area of the basal planes decreases, while that of the edges and defects increases significantly. XPS analyses were performed to probe the surface chemistry of the oxidized CNTs. The surface oxygen content was estimated based on the C 1s and O 1s peak intensities. Quantitative analysis shows that the oxygen content increases with the duration of the HNO_3 treatment (Table S2 and Fig. S2a†). Curve fitting of the O 1s peaks helped to identify three (minimum number of peaks) main O 1s components (Fig. 1 and Table S2†). The components associated to carbon correspond to C═O groups (531.5 ± 0.1 eV, including quinone, carbonyl, lactone, and C═O of carboxylic groups), C–OH and/or C–O–C groups (533.5 ± 0.1 eV, involving ether

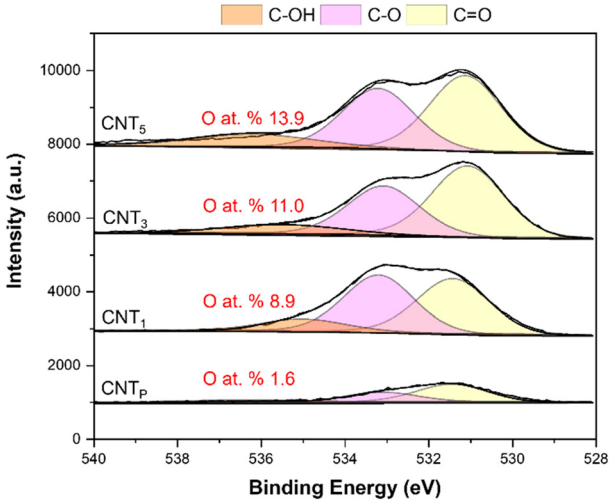

Fig. 1 High-resolution XPS O 1s spectra of the four CNT samples.

and hydroxyl groups bonded to aromatics/aliphatics), and C–OH of carboxylic groups (535.5 ± 0.1 eV).[31–35] The C═O/C–O peak area ratio decreases upon oxidation and the concentration of carboxylic groups increases. The increase of all types of OFGs (both CO_2- and CO-releasing groups) upon nitric acid oxidation was also confirmed by TPD-MS analyses (Fig. S3a†).

The TPD spectra of the CNTs show different CO_2 evolution maxima at ~230/270, 400/500 and ~600/650 °C (Fig. S4a†), corresponding to the desorption of carboxylic acids, carboxylic anhydrides and lactones, respectively.[36] For carboxylic acids, –COOH groups with varying acidities decompose at distinct temperatures, with the strongest acidic group undergoing decomposition at the highest temperature.[37,38] Noticeably, the CNT_1 sample shows a higher decomposition temperature of carboxylic groups (270 °C, Fig. S4b†) than the other samples (230 °C), suggesting the presence of stronger acidic sites on this sample. CO evolution is detected in a temperature range from ~300 °C to 900 °C, with the maximum located at ~800 °C. This broad signal corresponds to the superposition of the CO evolution associated to the decomposition of carboxylic anhydrides, phenolic, carbonyl (ketones, aldehydes, quinones) and ether (chromene) surface functional groups.[36]

Overall, these analyses show the increase of all types of OFGs upon HNO_3 oxidation as well as the opening of the CNT tips.

Synthesis and characterization of oleylamine-capped $Pd_{p\text{-}NP}$

The $Pd_{p\text{-}NP}$ were prepared using modified versions of the oleylamine-mediated synthesis.[39] Two batches of $Pd_{p\text{-}NP}$ were prepared according to published procedures to synthesize $Pd_{p\text{-}NP}$ of around 2.4 ($Pd_{2.4}$)[40] and 4.4 nm ($Pd_{4.4}$).[25] The $Pd_{2.4}$ nanoparticles (NPs) were prepared using a mixture of OAm and oleic acid as weak capping agents, whereas the $Pd_{4.4}$ NPs were prepared using pure OAm. The results of elemental analysis for the washed $Pd_{p\text{-}NP}$ are presented in Table S3.† As expected, the Pd content is higher for the $Pd_{4.4}$ sample. To estimate the coverage of Pd particles with OAm (Θ_{OAm}) in the two samples we first evaluate metal dispersion from a universal mathematical relation between the mean relative size of Pd_{NP} and their dispersion.[27] Then, we used the Pd and nitrogen content measured by ICP-OES and elemental analyses, respectively. The calculated N/Pd_{surf} atomic ratios (Θ_{OAm}) are reported in Table S3.† The values obtained, 0.36 for the $Pd_{2.4}$ sample and 0.30 for the $Pd_{4.4}$ sample, show not much difference between the two samples. To understand the nature of chemical/electronic interactions between the capping agent and $Pd_{p\text{-}NP}$, FTIR analyses were performed. Fig. S5† shows a series of FTIR spectra of free OAm and washed OAm-capped $Pd_{p\text{-}NP}$. The stretching vibrations of N–H can be detected at about 3450 cm^{-1} (3370 cm^{-1} for the free OAm).[41] The two peaks at 2853 and 2925 cm^{-1} represent the symmetric and asymmetric CH_2 stretching modes of the OAm carbon chain.[42] The peak at around 1637 cm^{-1} (1615 cm^{-1} for the free OAm) was assigned to the combined motion of NH_2 scissoring and N–H bending.[43] Bending vibration of the –C═C bond has also been proposed at 1647 cm^{-1} for pure OAm.[44] No contribution of the bidentate carboxylate group ($-COO^-$) of OAc binding on the Pd surface (at around 1540–1570 cm^{-1}) was noticed. This is an indication that the $Pd_{2.4}$ NPs should be mainly protected by OAm molecules and not by carboxylates from OAc, as already reported for similar $Pd_{p\text{-}NP}$.[40] To confirm this hypothesis we compared the C/N ratio (obtained by elemental analysis) of the $Pd_{2.4}$ and $Pd_{4.4}$ (prepared from pure OAm) NPs. This ratio is 15.4 for pure OAm, 14.5 for the $Pd_{4.4}$ NPs and 10.3 for the $Pd_{2.4}$ NPs. The ratio measured for the $Pd_{2.4}$ NPs confirms that OAm should be the main stabilizing ligand in these $Pd_{p\text{-}NP}$. A low-intensity peak at 1670 cm^{-1} could result from a condensation reaction between OAm and OAc giving rise to an amide.[45] However, the precise assignment of the amine groups (especially primary amine) is difficult due to the overlap of broad vibrational absorption bands of OH groups in the range of 3200–3500 cm^{-1} and at 1595 cm^{-1}. The peak at 1458 cm^{-1} (1465 cm^{-1} for the free OAm) is associated with the C–H bending mode.[42] The peak at 803 cm^{-1} is attributed to the N–H wagging peak of secondary amines,[46] and the peak at around 720 cm^{-1} has been assigned to a C–H ($C \geq 7$) flexural vibration.[47] These FTIR spectra provided supportive evidence that OAm is present on the surface of the as-prepared monodisperse $Pd_{p\text{-}NP}$. Actually, OAm is frequently used as a protecting ligand for Pd_{NP},[47,48] and the interaction between the N atom of secondary amines and surface Pd atoms has been reported.[49] The amine binds to the metal surface at the top site through the lone-pair electrons of the nitrogen atom.

XPS analyses were performed on the $Pd_{2.4}$ sample to probe the surface chemistry and oxidation state of Pd (Fig. S6†). Pd was observed in two oxidation states, including contributions corresponding to $Pd^{(0)}$ (335.8 eV, 67 at%, the theoretical Pd $3d_{5/2}$ binding energy (BE) of metallic Pd being 335.4 eV)[50] and Pd^{2+} (336.5 eV, 23 at%, the theoretical Pd $3d_{5/2}$ BE of

PdO being 336.8 eV)[50] in accordance with reported values in the literature.[51] The calculated Pd^0/Pd^{2+} ratio was 1.99. The N 1s peak was deconvoluted with two components. The major component (75%) at 399.7 eV is assigned to the N atom bound on the Pd surface. The component at 401.9 eV (25%) can be attributed to the presence of ammonium species, which could result from the reaction between OAm and OAc.[52,53] The calculated N/Pd atomic ratio was 0.23.

Transmission electron microscopy (TEM) images of the washed $Pd_{p\text{-}NP}$ (Fig. 2) showed that the $Pd_{2.4}$ and $Pd_{4.4}$ samples present a mean diameter of 2.4 and 4.4 nm, respectively, and a narrow size distribution. The $Pd_{2.4}$ NPs appear to be more agglomerated on the carbon-coated TEM grid compared to the $Pd_{4.4}$ ones.

This is related to their smaller size and lower stability induced by the presence of a weakly coordinating ligand (OAm),[54] because Pd as a soft acid interacts weakly with the amine, which is a hard base.

Overall, these analyses show that the preformed nanoparticles are mainly stabilized by weakly coordinating OAm ligands.

Synthesis and characterization of the supported catalysts

The colloidal $Pd_{p\text{-}NP}$ were deposited on the CNT supports following a simple impregnation procedure in pentane. The presence of dispersed $Pd_{p\text{-}NP}$ on CNTs was probed by XRD (Fig. S7†) and TEM (Fig. 3) for the $Pd_{2.4}$/CNT samples. Fig. S7† shows the XRD patterns of the supports and supported $Pd_{2.4}$ NPs. The low Pd loading (around 1% (w/w), Table 1) and/or the small size of the $Pd_{p\text{-}NP}$ should be at the origin of the absence in the XRD pattern of the supported catalysts of the expected characteristic (111) and (200) diffraction peaks of Pd at 40.0° and 46.6°, respectively. Fig. 3 shows representative images of the $Pd_{2.4}$ NPs after deposition on the CNTs. The particle size distributions are shown in Fig. S8† and representative HR-TEM micrographs in Fig. S9.† The TEM micrographs show that the particles are not distributed uniformly on the carbon support and have the tendency to agglomerate. The clustering of small $Pd_{p\text{-}NP}$ prepared from OAm on the CNT surface has already been reported.[55] This clustering is not the result of the immobilization procedure. Indeed, as shown by the TEM micrographs of free-standing $Pd_{2.4}$ NPs (Fig. 2), aggregation is already obvious in their suspension due to their stabilization by weakly coordinating ligands. Regarding the mean particle size of supported $Pd_{2.4}$ nanoparticles, a slight increase was measured in the case of the $Pd_{2.4}/CNT_5$ sample. This could be related to the fact that on the more oxidized CNTs, the presence of a high concentration of surface carboxylic groups favors a reaction with the stabilizing OAm ligands to form surface grafted quaternary ammonium carboxylate salts, depriving the NPs of their stabilizer.[56–58]

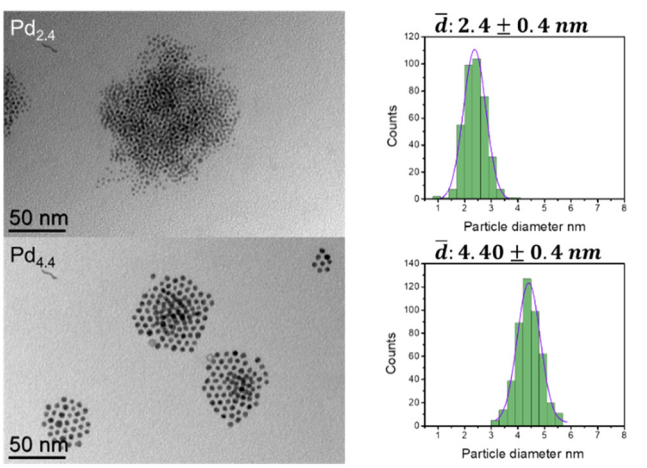

Fig. 2 TEM images of the monodispersed 2.4 ± 0.4 nm and 4.4 ± 0.4 nm $Pd_{p\text{-}NP}$.

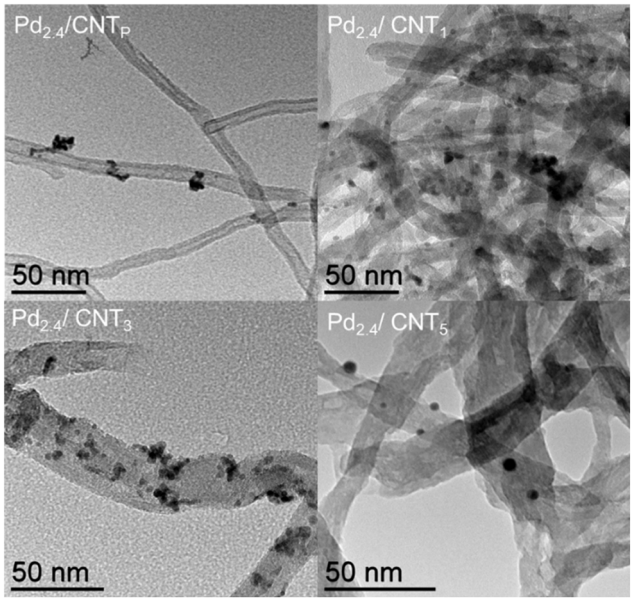

Fig. 3 TEM images of the CNT-supported $Pd_{2.4}$ nanoparticles.

This lower Θ_{OAm}, resulting from spillover of the OAm ligand on the support, should favor sintering. The possibility of spillover of basic amine ligands from metal NPs onto acidic oxide supports has already been mentioned in the literature.[59,60] This in an important phenomenon that can influence not only NP size but also reactivity. In a similar work, evidence that polyvinylpyrrolidone used as a stabilizing agent for gold colloids was present on both the metal and the support surface after colloid deposition on a TiO_2 support was also provided.[61] In the case of oxidized carbon materials, it is worth mentioning that the presence of surface carboxylic groups with varying acidities has been reported (distributed over a wide pK_a range between 2 and 9),[37,38] which suggests that the spilt-over amine ligands will interact more or less strongly according to the acidity of the –COOH groups.

The CNT-supported $Pd_{4.4}$ NPs were also characterized by ICP-OES and TEM (Table 1 and Fig. S10†). In that case, the larger and more stable $Pd_{4.4}$ NPs appear to be more uniformly distributed on the CNT supports, and no

Table 1 Characterization of the supported catalysts

Catalyst	Pd loading[a] (%)	P_{NP} size (nm)	$Pd_{surf.}$ (at%)	XPS Pd $3d_{5/2}$ peak (BE/eV) Pd^0	XPS Pd $3d_{5/2}$ peak (BE/eV) Pd^{2+}	Pd^0/Pd^{2+}
$Pd_{2.4}/CNT_P$	1.16	2.6 ± 0.6	0.60	335.6	337.3	2.48
$Pd_{2.4}/CNT_1$	0.81	2.7 ± 0.5	0.11	335.5	337.3	1.76
$Pd_{2.4}/CNT_3$	0.90	2.5 ± 0.9	0.88	335.7	337.4	2.98
$Pd_{2.4}/CNT_5$	1.16	3.2 ± 0.8	0.65	335.5	337.2	1.85
$Pd_{4.4}/CNT_P$	1.04	3.9 ± 0.5	—	—	—	—
$Pd_{4.4}/CNT_1$	1.01	4.0 ± 0.5	—	—	—	—
$Pd_{4.4}/CNT_3$	1.07	4.2 ± 0.6	—	—	—	—
$Pd_{4.4}/CNT_5$	1.06	3.9 ± 0.6	—	—	—	—
Pd_{NP}/CNT_1	0.51	2.1 ± 0.6	0.18	335.9	337.6	1.33
Pd_{NP}/CNT_3	0.54	2.0 ± 0.6	0.16	335.9	337.6	1.49
Pd_{NP}/CNT_5	0.73	2.0 ± 0.4	0.17	335.8	337.5	3.13

[a] Determined by ICP-OES.

significant variation of the mean particle size was measured (3.9–4.2 nm). FTIR analyses performed on the supported $Pd_{2.4}$ nanoparticle series (Fig. S11†) show very weak bands related to OAm at 2856 and 2929 cm^{-1}. XPS analyses were performed on the supported $Pd_{2.4}$ nanoparticle series to determine the surface elemental composition of these samples. As shown in Fig. 4a, all Pd 3d XPS spectra can be deconvoluted into two pairs of doublets.

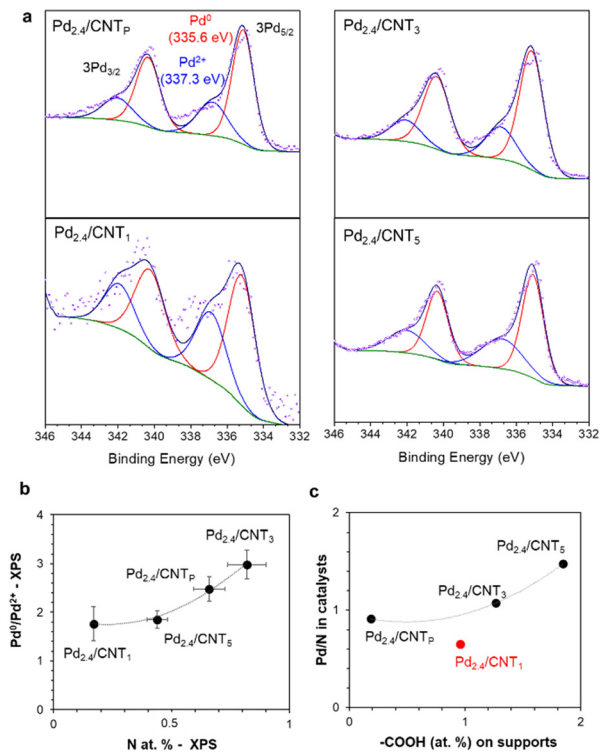

Fig. 4 (a) High-resolution XPS spectra of the Pd 3d region of the CNT-supported $Pd_{2.4}$ nanoparticles. (b) Correlation between the at% of nitrogen measured by XPS and the Pd^0/Pd^{2+} ratio for the CNT-supported $Pd_{2.4}$ nanoparticle series. (c) Evolution of the Pd/N ratio in the CNT-supported $Pd_{2.4}$ nanoparticles with the concentration of carboxylic groups on the bare supports.

The Pd was observed in various oxidation states, including contributions corresponding to bulk Pd metal (335.5 eV, 64–75 at% according to the samples) and oxidized species (337.3 eV). This latter BE is consistent with the values reported in the literature for Pd^{2+} (336.3–336.9 eV, 25–36 at% according to the samples).[62] This peak can be attributed to surface oxide PdO_{surf} resulting from air oxidation[63] and/or to a charge transfer from Pd to the oxidized carbon support.[62] Considering the surface Pd content (Table 1), it is noticeable that the $Pd_{2.4}/CNT_1$ sample contains much less Pd on the CNT surface. It can be considered that a larger proportion of the $Pd_{p\text{-}NP}$ in this sample could be located inside the CNT cavity[64] as it is known that the HNO_3 treatment opens the CNT tips. The lower concentration of OFGs on CNT_1 compared to CNT_3 and CNT_5 should minimize the interaction of the OAm ligands and carboxylic groups, which concentrate at the CNT tips,[65] thus favoring the confinement of $Pd_{p\text{-}NP}$. The evolution of the atomic Pd/C, Pd/N, Pd/O and C/N ratio as determined by XPS (Fig. S12†) supports this hypothesis. Sample-dependent variations in the Pd^0/Pd^{2+} ratio were also evidenced (Table 1). An increase in the Pd^{2+} content was observed for samples $Pd_{2.4}/CNT_1$ and $Pd_{2.4}/CNT_5$. Such an increase could be related to a lower Θ_{OAm} of the $Pd_{2.4}$ nanoparticles in these two samples, which should favor the exposure of the samples to oxygen from air. A lower Θ_{OAm} should also limit the electron donation from OAm to Pd, strengthening the effect of charge transfer from Pd to the support. Both effects should contribute to increase the Pd^{2+} content. Even though the at% of nitrogen determined by XPS on this catalyst series does not directly reflect the Θ_{OAm}, we tried to correlate it with the Pd^0/Pd^{2+} ratio (Fig. 4b). A fairly good correlation was obtained.

The N 1s spectra of the CNT-supported $Pd_{2.4}$ nanoparticles are given in Fig. S13.† For the four samples, the main components, at 400.0–401.0 eV according to the sample, are quite broad and present a fairly large FWHM of 3.4–3.5 eV, suggesting multicomponent composition. These BEs are consistent with the ones reported in the literature for OAm interacting weakly with the surface of NPs.[66–68] A

contribution can also be expected at lower BE (398.2 eV) from the C–N bond between an aliphatic carbon and the nitrogen of the amine group.[69] A shift of the N 1s XPS peak to higher BE (401.5 eV) may be related to the presence of carboxylate derivatives (interaction between OAm and surface carboxylic groups).[70] The significant presence of amide groups (BE 399.9 eV)[71] formed from the condensation reaction of carboxylic acids with OAm is unlikely considering that the catalysts were prepared at room temperature. Considering the low intensity of the observed peaks, no deconvolution was performed on these spectra. The evolution of the atomic Pd/N ratio in these samples was analyzed to obtain information on the fate of the OAm ligand during $Pd_{p\text{-}NP}$ deposition. The $Pd_{2.4}/CNT_1$ sample was not considered in this analysis since in that case a significant amount of $Pd_{p\text{-}NP}$ should be confined in CNT_1. The Pd/N ratio is increasing in the order $Pd_{2.4}/CNT_5 > Pd_{2.4}/CNT_3 > Pd_{2.4}/CNT_P$. This means that upon $Pd_{p\text{-}NP}$ deposition, more OAm is immobilized on the more oxidized CNT_5. In fact, a reasonable correlation was found between the Pd/N ratio and the amount of –COOH groups, both determined by XPS (Fig. 4c). A possible explanation of this tendency is that upon $Pd_{p\text{-}NP}$ deposition, spillover of OAm occurs to form ammonium carboxylates with the –COOH of the support. This phenomenon should be more pronounced on the samples showing the higher concentration in –COOH groups ($CNT_5 > CNT_3 > CNT_P$). The washing procedure performed in EtOH after $Pd_{p\text{-}NP}$ deposition should more easily remove part of the OAm arising from these ammonium carboxylates (restoring the –COOH groups) than from the OAm ligands on the Pd surface.[72] As far as the $Pd_{2.4}/CNT_1$ sample is concerned, it is out of the trend.

For this sample, the Pd/N ratio is quite low, suggesting that the reaction of OAm with surface –COOH groups is not occurring in the inner cavity of CNT_1, since the inner cavity of CNTs should not be functionalized by OFGs.[73] The O 1s spectra of the CNT-supported $Pd_{2.4}$ nanoparticles are given in Fig. S14 and the data from deconvolution in Table S4 and Fig. S2b.†

Compared to the bare supports (Fig. 1 and S2a†), it is noticed that (i) the O content is higher on $Pd_{2.4}/CNT_P$ than on the corresponding bare support, while it is lower for the other samples, and (ii) the relative C═O/C–O ratio is lower for the CNT-supported $Pd_{2.4}$ nanoparticles than for the bare supports.

Finally, TPD-MS analyses were also performed on the CNT-supported $Pd_{2.4}$ nanoparticles (Fig. S3b†). Compared to the bare supports (Fig. S3a†), we noticed as a general trend that the CO_2-releasing groups have the tendency to disappear on the supported catalyst, particularly in the 200–400 °C temperature range. This disappearance is accompanied by the production of water in the same temperature range. This phenomenon can be rationalized by a series of reactions involving the OAm ligand and the CO_2 releasing groups, all of them involving the release of H_2O (Fig. S15†).[74] The resulting N-containing surface groups will further decompose to produce hydrogen cyanide as a decomposition product at various temperatures: >900 °C for pyridinic groups, ~800 °C for pyrrolic groups, and ~250 °C for nitrile groups.[75] For the $Pd_{2.4}/CNT_5$ catalyst, the CO_2 profile shows the appearance of an intense and narrow peak at ~600 °C, a temperature that corresponds to the decomposition of lactonic groups.[37] The formation of these groups could result from Pd-catalyzed lactonization of carboxylic acids.[76] The fact that this peak is relatively narrow suggested a catalytic decomposition of these groups that should be close to Pd. To further examine the fate of the OAm ligand, the mass corresponding to N-containing species potentially resulting from decomposition of adsorbed OAm was followed (Fig. S16† for NH_3, HCN, NO and NO_2). Under an inert atmosphere, free oleylamine decomposes at 200–300 °C, while when it is adsorbed on metal NPs, its decomposition requires higher temperatures.[47,77,78] For OAm-capped Pd_{NP}, the decomposition occurs between 200 and 500 °C.[47] Upon heating, the desorption of amines from metal particles competes with their dehydrogenation. The thermal decomposition of primary amines adsorbed on metallic surfaces should produce first HCN (by dehydrogenation) and then NH_3 (by hydrogenation) as decomposition products.[79] Since the total m/z = 17 profile included contributions from both NH_3 and OH, we concentrate our analysis on HCN evolution (Fig. S16b†). The HCN evolution patterns presented in Fig. S16b† show, for the four samples, a broad desorption peak between 300 and 550 °C. We have attributed this peak to the thermal decomposition of OAm adsorbed on the Pd surface. A second peak centered at around 200 °C is also observed, mainly for samples $Pd_{2.4}/CNT_P$ and $Pd_{2.4}/CNT_1$. This peak may result from free OAm or OAm interacting weakly with the support on poorly functionalized regions. A contribution from the decomposition of some nitrile groups formed during the reaction of OAm with –COOH groups (Fig. S15†), which decompose at around 250 °C by liberating HCN, can also be envisaged.[75] Finally, a third peak is detected at T <100 °C, particularly in samples $Pd_{2.4}/CNT_1$ and $Pd_{2.4}/CNT_3$. Such a low-temperature peak could result from a specific mode of decomposition of ammonium carboxylates not removed by the washing step, presumably the most stable ones resulting from the reaction of OAm with the more acidic –COOH groups (Fig. S4b†). It is also possible to envisage a catalytic decomposition of these surface groups located near palladium, as proposed for some oxygen functional groups.[19,80]

The characterization results obtained show that the deposition of $Pd_{p\text{-}NP}$ on carbon nanotubes by a simple impregnation method significantly changes the surface chemistry of the supports and the particles. This is particularly true for the smaller and less stable $Pd_{2.4}$ nanoparticles (Scheme 1), for which the weakly bound OAm ligands can react with –COOH groups of the support (ligand spillover), as strongly suggested by XPS and TPD-MS analyses. According to the strength of the –COOH groups, the spilt-over OAm may either be removed during the washing steps of the catalyst or remain on the support surface. This phenomenon in turn contributes to modifying not only the size of the Pd particles, as shown in the $Pd_{2.4}/CNT_5$ sample,

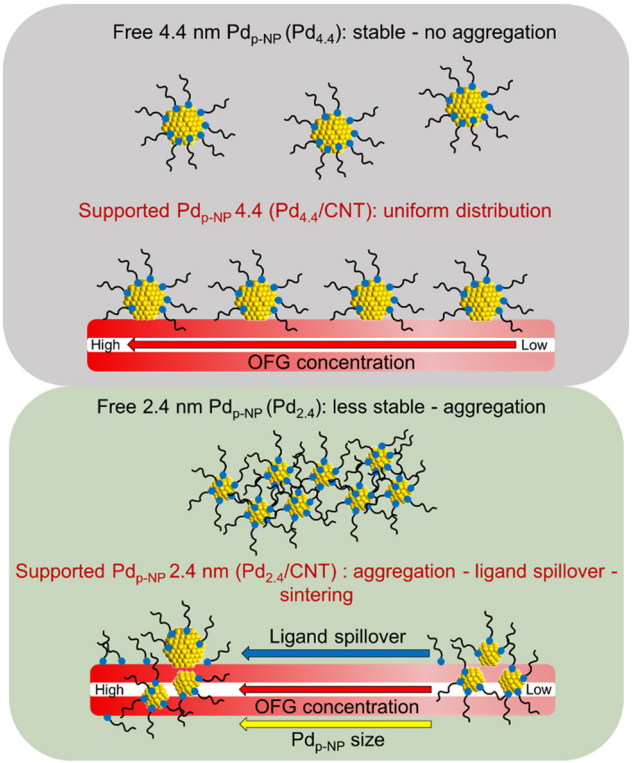

Scheme 1 Representation of the evolution of $Pd_{p\text{-}NP}$ distribution on the CNT surface according to the size of the $Pd_{p\text{-}NP}$ (2.4 or 4.4 nm) and OFGs concentration.

but also the Pd^0/Pd^{2+} ratio, which is known to impact hydrogenation performance.[81–83] Taken together, these results suggest that using preformed particles to decorrelate the influence of OFGs from that of the metal dispersion and its oxidation state on catalytic performance may not be such a straightforward task.

Phenylacetylene hydrogenation

The elimination of PhA, an impurity present in ST, by selective semi-hydrogenation into ST, is a process of industrial relevance since PhA poisons and deactivates polymerization catalysts in polystyrene production plants. Thermodynamic and/or kinetic parameters, which depend on catalyst formulation, can influence this challenging transformation. In addition, for colloidal nanoparticles, the balance between the adsorption energetics of substrates/intermediates and capping ligands also contribute to the activity and selectivity of catalysts.[84] Different levers can be employed to improve the catalytic performance of carbon-supported Pd catalysts for this reaction, such as (i) controlling the metal particle-size[85–87] or Pd phase,[88] (ii) adding a second metal,[89–91] or (iii) changing the surface chemistry of the carbon support.[20,92–94] As stated in the introduction, some of these parameters can be interconnected. Thus, increasing the concentration of OFGs can positively affect Pd dispersion, which in turn dictates the catalytic performance.[20,95] In the present study, Pd dispersion and oxidation state, OFG density and Θ_{OAm} are the relevant parameters that can influence the catalytic performances. Serp *et al.* discussed the influence of Pd dispersion on catalyst performances for PhA hydrogenation[87] and proposed that different size ranges should be considered. On large Pd_{NP}, the formation of the β-PdH phase is believed to contribute to alkyne over-hydrogenation. For smaller Pd_{NP}, on which the number of low-coordinated Pd atoms are starting to compete with the Pd(111) surface atoms, the stronger ST adsorption energy with decreasing Pd_{NP} size induces a decrease in selectivity (electronic effect based on donation/back donation). Finally, for Pd clusters, the ST adsorption weakens rapidly due to a geometric effect, with a decrease in size up to Pd single atoms (Pd_{SA}). Cooperative catalysis between Pd nanoparticles or clusters and Pd_{SA} has also been proposed to operate on various supports.[87,96] As far as the influence of OFGs is concerned, it was proposed that a high density of OFGs favors the formation of small Pd_{NP}, exhibiting mainly edge and corner sites along with Pd/OFG interfaces as primary active sites.[20] Such Pd_{NP} were reported to be less active than the larger ones obtained on supports presenting a low density of OFGs. It is intriguing that a reverse tendency was reported for Pt_{NP} deposited on CNTs.[97] However, differentiating the impacts of Pd_{NP} size (size effect) from variations in the quantity of OFG interfacial sites (interfacial effect) on catalytic performance is a challenge.

The catalytic performance for PhA selective hydrogenation to ST was evaluated for the different catalysts at 30 °C under 5 bar H_2 in methanol with a PhA/Pd molar ratio of 10 000. A stirring rate of 1000 rpm ensured that the hydrogenation tests were performed under a regime without mass transfer limitations. All reactions were performed up to 100% conversion. Most of the reactions were repeated twice to ensure the reproducibility of the results. The evolution of STY_{100} and $S_{ST\text{-}100}$ for the different catalysts is given in Fig. 5 (see Fig. S17† for values at 20% and 90% conversion). For the $Pd_{2.4}$ nanoparticles, it is first shown that the supported $Pd_{p\text{-}NP}$ showed increased activity compared to the unsupported ones. This should be related to a stabilization effect from the carbon support that limits the aggregation/sintering of the $Pd_{2.4}$ nanoparticles during catalysis.[98] To confirm this hypothesis TEM analyses were performed on the used $Pd_{2.4}$, $Pd_{2.4}/CNT_3$ and $Pd_{4.4}/CNT_3$ catalysts (Fig. S18†). The results obtained clearly evidence a severe aggregation of the $Pd_{2.4}$ free NPs, which can explain their poor performances.

If we consider the effect of Pd_{NP} size on catalyst activity, it seems that globally the smaller $Pd_{p\text{-}NP}$ are the more active, the only notable exception being for the more oxidized CNT_5 support for which $Pd_{4.4}$ and $Pd_{2.4}$ performed similarly. To check if this could be related to the higher surface area of the supported $Pd_{2.4}$ nanoparticles compared to the $Pd_{4.4}$ ones, we calculated a TOF integrating the Pd dispersion and the ligand coverage estimated from the values obtained for the free $Pd_{p\text{-}NP}$ (Table S2†) to access the accessible Pd surface. This calculation

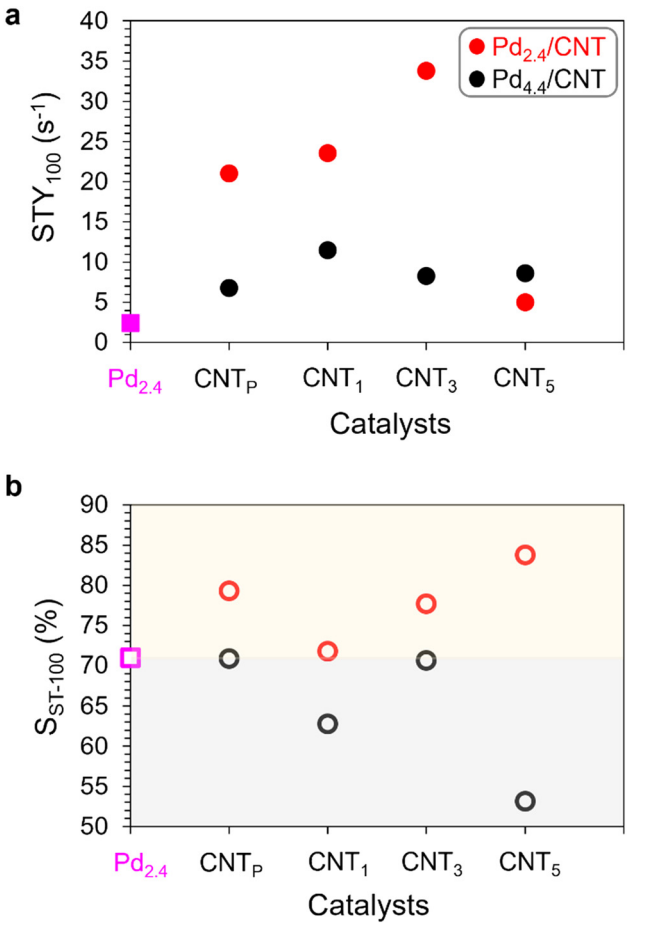

Fig. 5 Evolution of (a) site time yield and (b) styrene selectivity according to the catalyst type (free-standing $Pd_{2.4}$ NPs, $Pd_{2.4}$/CNT and $Pd_{4.4}$/CNT series) for phenylacetylene hydrogenation at 100% conversion.

does not consider any ligand spillover upon $Pd_{p\text{-}NP}$ deposition. The values obtained (Fig. S19†) mean that the STY cannot be only related to the exposed Pd surface area. A plausible explanation of this result could arise from a different Θ_{OAm} on the $Pd_{p\text{-}NP}$, according to their size and also to the density of OFGs. As the spillover effect should principally involve perimeter surface sites, it could be more significant for the $Pd_{2.4}$ NPs. As capping agents are often postulated to block some active sites or to act as an energy barrier in surface reactions on transition metal nanoparticles,[99] a lower ligand coverage should favor the activity.

The spillover of the OAm ligand should be also favored on supports presenting a higher concentration of carboxylic surface groups. The significant differences of catalyst activity observed between the $Pd_{2.4}/CNT_P$, $Pd_{2.4}/CNT_1$ and $Pd_{2.4}/CNT_3$ samples could be related to this phenomenon. But this cannot explain the low activity of the $Pd_{2.4}/CNT_5$ catalyst, which should present an even lower Θ_{OAm}. We also analyzed the effect of the $Pd^{(0)}/Pd^{2+}$ ratio, which itself depends on the atomic % of nitrogen (Fig. 4b), on the activity (Fig. S20a†), since a high $Pd^{(0)}$ content should allow an increased hydrogenation activity.[82] An excellent correlation was obtained including the $Pd_{2.4}/CNT_P$, $Pd_{2.4}/CNT_3$ and $Pd_{2.4}/CNT_5$ catalysts, but the $Pd_{2.4}/CNT_1$ catalyst is breaking the trend. This could be related to the fact that a significant amount of $Pd_{2.4\text{-}NP}$ should be confined in this catalyst. Therefore the low activity of the $Pd_{2.4}/CNT_5$ catalyst could be related to its low $Pd^{(0)}/Pd^{2+}$ ratio. In the case of the $Pd_{4.4}$/CNT series, the fact that OAm spillover should be reduced could explain that the OFG density does not significantly affect the catalyst activity.

If we consider the effect of Pd_{NP} size on catalyst selectivity, it appears that the smaller supported $Pd_{p\text{-}NP}$ are more selective towards ST. An increase in ST selectivity is generally associated to a lower adsorption energy of the ST molecule on the metal surface. Differences in ST adsorption strength could arise not only from a particle size effect, as discussed above,[87,100] or from the chemical state of Pd,[101,102] but also from stabilizing ligand effects.[84] Considering the small size of $Pd_{p\text{-}NP}$ in the $Pd_{2.4}$/CNT catalysts, and assuming that Pd_{NP} <2 nm do not form the hydride phases,[102] we can propose that the lower S_{ST} obtained on the $Pd_{4.4}$/CNT catalysts could be due to the presence of the β-PdH phase. Such a phase is formed for 4 nm Pd particles.[103,104] On the other hand, the evolution of ST adsorption energy with the presence of capping ligands is difficult to appreciate since it should evolve both with Θ_{OAm} and with adsorption strength of the ligand. In our case, the Θ_{OAm} should be higher for the $Pd_{4.4}$/CNT catalysts, but the OAm ligand should be adsorbed stronger on the smaller $Pd_{p\text{-}NP}$ of the $Pd_{2.4}$/CNT catalysts.[105] To evaluate the influence of OFG density on ST selectivity, we have focused on the more selective $Pd_{2.4}$/CNT catalysts. As the $Pd^{(0)}/Pd^{2+}$ ratio can impact the selectivity in alkyne hydrogenation reactions,[81] this parameter was used to establish a possible correlation with the S_{ST}. While the correlation obtained (Fig. S20b†) is reasonably good for the $Pd_{2.4}/CNT_P$, $Pd_{2.4}/CNT_3$ and $Pd_{2.4}/CNT_5$ catalysts, it is obvious that there also, the $Pd_{2.4}/CNT_1$ catalyst is breaking the trend. The fact that a significant amount of $Pd_{p\text{-}NP}$ should be confined in this catalyst could be at the origin of this discrepancy.

The stability of the supported preformed Pd nanoparticles during catalysis was evaluated with the $Pd_{2.4}/CNT_3$ catalyst, which shows a good balance between activity and selectivity. Fig. S21† shows the performance of this catalyst during 7 recycling tests. There is a decrease of PhA conversion and styrene selectivity upon recycling, which might be due to Pd sintering, as verified by TEM analyses on the spent catalyst (Fig. S22†). In order to verify whether these results could also be related to catalyst losses during recycling operations, a test was carried out using all the liquid phases obtained after filtration of the catalyst. After concentration and addition of PhA to this concentrated filtrate, a new hydrogenation test was carried out. The results of this test (Fig. S23†) show a very low activity (complete PhA conversion after more than 1300 min), which may be related to the presence of palladium in the solution.

To further investigate the role of the $Pd^{(0)}/Pd^{2+}$ ratio on the S_{ST} selectivity and to eliminate the possible influence of the OAm ligands, we also prepared a series of Pd_{NP}/CNT catalysts by conventional impregnation from Pd nitrate on

CNT_1, CNT_3 and CNT_5. In contrast to what was expected from the literature, at such a low Pd loading (1% (w/w)), we did not find significant differences in the mean Pd_{NP} size for these three catalysts (see Fig. S24† for TEM micrographs and particle size distribution), which all present an average Pd_{NP} diameter of 2 nm.

The XPS characterization (Fig. S25 for Pd 3d, Fig. S26 for O 1s, Fig. S2c, Table S4† and Table 1) shows that for this catalyst series, the $Pd^{(0)}/Pd^{2+}$ ratio is increasing with the at% of oxygen present on the bare supports, the higher ratio being obtained on CNT_5 (Fig. S27a†). Such a tendency was not observed for the $Pd_{2.4}$/CNT series (Fig. S27b†). Contrasting results have been reported in the literature related to the effect of OFG density on the $Pd^{(0)}/Pd^{2+}$ ratio. The research groups of Hutchings[106] and Wang[107] reported a decrease of the $Pd^{(0)}/Pd^{2+}$ ratio when increasing the at% of oxygen on the support. XRD, TEM, XPS and H_2-TPR analyses indicated that the presence of surface carboxylic groups could effectively inhibit the sintering and reduction of Pd^{2+} species.[107] An opposite tendency, similar to the one obtained in the present study, was reported in other studies.[18,108] Thus, Tessonnier *et al.* proposed that the observed increase in the $Pd^{(0)}/Pd^{2+}$ ratio in Pd/CNT catalysts when increasing the concentration of OFGs is related to the increased work function of the oxidized supports. Indeed, it has been shown that carbonyl and carboxyl groups are the dominant contributors to the increase in the work function of CNTs.[109] Therefore, these results suggest that the $Pd^{\delta+}$ phase arises from the difference in the position of the Fermi levels of functionalized carbon supports and Pd_{NP}, which affects the charge transfer. To conclude on the evolution of the Pd^{2+}/Pd^0 ratio in the prepared samples (preformed particles of 2.4 nm diameter, $Pd_{2.4}$/CNT series, and particles of 2 nm obtained by impregnation, Pd_{NP}/CNT series) it appears that two main parameters can influence this ratio: the surface coverage in the stabilizing ligand and the at% of oxygen present on the bare supports. For the $Pd_{2.4}$/CNT series, the first parameter is the most important, while for the Pd_{NP}/CNT series, only the second parameter is relevant.

The BE of $Pd^{(0)}$ in this catalyst series is upshifted (335.8–335.9 eV) as compared to the $Pd_{2.4}$/CNT catalyst series (335.5–335.7 eV), suggesting a different metal–support interaction. Charge transfer from Pd to the support should create globally electrodeficient Pd particles. Recent modeling studies on supported catalysts, in which Bader charges were calculated, agreed with the fact that charge depletion is in fact limited at the metal/support interface (Pd^{2+} region in Scheme 2a), whereas charge accumulation is located on the top of the particles (Pd^0 region in Scheme 2a).[110–113] For $Pd_{2.4}$/CNT and Pd_{NP}/CNT catalysts, which present similar particle sizes, the charge transfer should be similar, leading to similar charge redistribution over the Pd particles. However, the presence of electron-donating OAm ligands[114,115] in the $Pd_{2.4}$/CNT catalysts should modify the charge redistribution, resulting in a lower Pd $3d_{5/2}$ binding energy than in the case of the

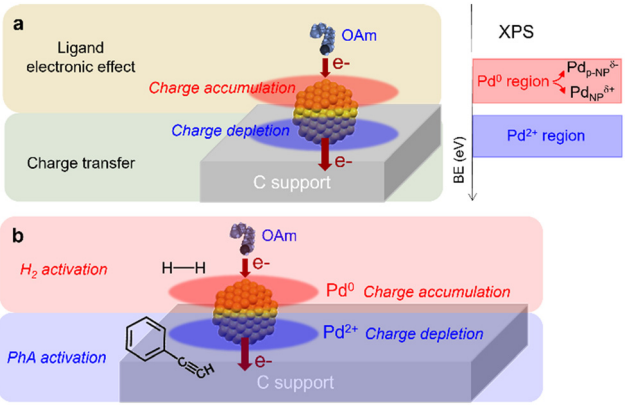

Scheme 2 (a) Model for charge redistribution in Pd/C catalysts based on charge transfer and electronic ligand effect. (b) Model of dual $Pd^{(0)}$ and Pd^{2+} site catalyzed mechanism involving H_2 and PhA activation.

Pd_{NP}/CNT catalysts. The relative atomic oxygen contents are similar in the Pd_{NP}/CNT and $Pd_{2.4}$/CNT catalyst series, but the distribution of OFGs is different (Fig. S2†).

This might be related to the fact that solutions of Pd nitrate used for the preparation of the Pd_{NP}/CNT catalyst series have oxidizing properties. In consequence, they will react with carbon surfaces to create new surface OFGs.[19,116]

The catalytic performances of this catalyst series are shown in Fig. S28,† where they are compared to those of the $Pd_{2.4}$/CNT catalyst series showing similar Pd particle size. The Pd_{NP}/CNT samples are globally less active and less selective than the $Pd_{2.4}$/CNT catalysts. The effect of the $Pd^{(0)}/Pd^{2+}$ ratio on STY and ST selectivity was compared for these two series of catalysts, not taking into account the $Pd_{2.4}/CNT_1$ catalyst (Fig. 6). While a significant influence of the $Pd^{(0)}/Pd^{2+}$ ratio on STY was observed for the $Pd_{p\text{-}NP}$ of the $Pd_{2.4}$/CNT series, it is not the case for the Pd_{NP}/CNT series (Fig. 6a). The lower activity of the Pd_{NP}/CNT catalysts could be tentatively attributed to the absence of the electron-donating effect of OAm,[115] which enriches the Pd with electrons (Pd^0 region in Scheme 2a) and should contribute to an easier H_2 activation. On the other hand, the effect of the $Pd^{(0)}/Pd^{2+}$ ratio on selectivity is the same for both catalyst series: an increase in the $Pd^{(0)}/Pd^{2+}$ ratio leads to a decrease in selectivity (Fig. 6b).

This can be rationalized if we consider the presence of dual Pd^{2+} and $Pd^{(0)}$ sites,[117] where $Pd^{(0)}$ should mainly contribute to the dissociation of H_2 and Pd^{2+} to the adsorption of the electron-rich C≡C bond (Scheme 2b).[81] An optimized $Pd^{(0)}/Pd^{2+}$ ratio should therefore be found to avoid over-hydrogenation. To confirm that the Pd^{2+} content was pivotal to reach high ST selectivity, we independently prepared a very low Pd loading catalyst on CNT_5 (0.07% (w/w)) from Pd nitrate. This catalyst contains mainly isolated Pd_{SA} and very few clusters (Fig. S29†) and should contain very few $Pd^{(0)}$.[87,118] The Pd_{SA}/CNT_5 catalyst is less active but more selective than the Pd_{NP}/CNT_5 catalyst (Fig. S30†). However, the $Pd^{(0)}/Pd^{2+}$ ratio itself cannot be used to rationalize the higher styrene selectivity obtained with the $Pd_{2.4}$/CNT catalyst series. Therefore, the balance between the adsorption

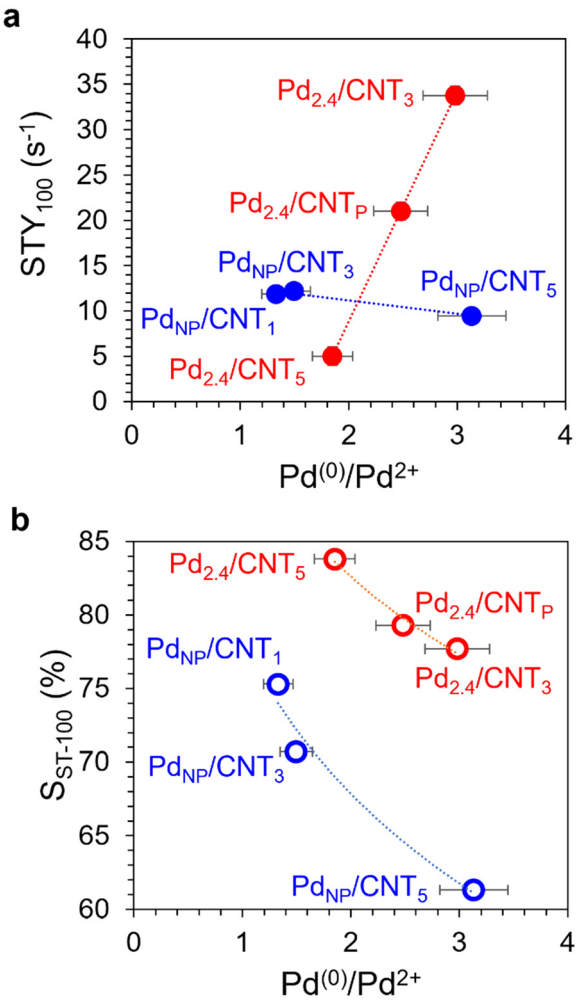

Fig. 6 Evolution of site time yield and styrene selectivity according to $Pd^{(0)}/Pd^{2+}$ ratio in the $Pd_{2.4}$/CNT (red marks) and Pd_{NP}/CNT catalyst (blue marks) series.

energetics of ST and the OAm capping ligand should also contribute to the selectivity. In the case of Pt particles for 4-octyne hydrogenation, Shevchenko *et al.* have shown that increasing 1-octylamine coverage on the Pt surface leads to the decrease in the binding energy of octenes.[84] Therefore, the higher selectivity obtained with the $Pd_{2.4}$/CNT catalysts could also be related to the presence of OAm. The electrons partially transferred from the OAm to the Pd particles, which increase the electronic density on Pd, may contribute to a weak ethylbenzene adsorption on the catalyst surface.[119]

The influence of the OAm ligand was evaluated in the case of the Pd_{NP}/CNT_1 catalyst by adding a known OAm amount (similar to the one measured for the $Pd_{2.4}$ NPs) on the reduced Pd_{NP}/CNT_1 catalyst. If we compare the catalytic performances of the Pd_{NP}/CNT_1 catalyst in the presence or absence of OAm (Fig. S31†), it can be concluded that on this catalyst, the addition of OAm induces an increase of activity but a decrease of selectivity. The fact that the activity is increasing upon OAm addition means that the blocking of active sites by the ligand should not be very significant. This might be related to the fact that OAm is a weak coordinating ligand for Pd compared to the alkyne. Therefore, the addition of OAm to the Pd_{NP}/CNT_1 catalyst should mainly contribute to a better H_2 activation, resulting in an increase in activity and a decrease in selectivity.

Finally, the influence of the spatial gradient of $Pd_{p\text{-}NP}$ was also evaluated in the case of the $Pd_{2.4}/CNT_5$ catalyst. Metal NPs' spatial distribution in supported catalysts is conventionally not quantified, and the influence of this collective property on catalyst performance remains poorly investigated.[120–122] For this, three catalysts were prepared with Pd loadings of 0.3%, 0.6% and 1.1% (w/w). TEM micrographs and particle size distribution of these three catalysts are shown in Fig. S32.† They present a similar Pd particle size of around 3 nm. Elemental analyses and ICP-OES results are shown in Table S6.† The PhA hydrogenation was performed either at iso-quantity of catalyst (varying the amount of PhA) or at iso-quantity of PhA (varying the amount of catalyst), keeping the PhA/Pd molar ratio at 10 000. The conversion *versus* time of these two series of experiments is shown in Fig. S33.† The same tendency is observed for both series of experiments: the $1.1Pd_{2.4}/CNT_5$ catalyst is much less active than the low-loading catalysts presenting the same CNT_5 support and similar Pd particle size. The STY and styrene selectivity were compared at 20%, 90% and 100% conversion for the series performed at iso-quantity of catalyst (Fig. S34†). Whatever the PhA conversion, the $1.1Pd_{2.4}/CNT_5$ catalyst is less active than the $0.6Pd_{2.4}/CNT_5$ and $0.3Pd_{2.4}/CNT_5$ catalysts, which both present similar STY. As far as ST selectivity is concerned, the $0.3Pd_{2.4}/CNT_5$ catalyst is the less selective, while the $0.6Pd_{2.4}/CNT_5$ and $1.1Pd_{2.4}/CNT_5$ catalysts performed similarly. From the results shown in Fig. 6 and S20,† this order of catalytic performance should reflect the $Pd^{(0)}/Pd^{2+}$ ratio (and thus the at% of N) in this catalyst series. The more active catalyst ($0.3Pd_{2.4}/CNT_5$), which should present the higher $Pd^{(0)}/Pd^{2+}$ ratio, is also the less selective. The fact that this catalyst is the one with the lowest loading should mean that less OAm should be released from the $Pd_{2.4}$ particles of the $0.3Pd_{2.4}/CNT_5$ catalyst during $Pd_{p\text{-}NP}$ deposition. This is confirmed by the $N/Pd_{surf.}$ atomic ratio values shown in Table S6† (values determined in a similar way as for Table S3†), for which the $0.3Pd_{2.4}/CNT_5$ sample shows the higher $N/Pd_{surf.}$ ratio. The evolution of STY_{100} and $S_{ST\text{-}100}$ with the values of this ratio for the $1.1Pd_{2.4}/CNT_5$, $0.6Pd_{2.4}/CNT_5$ and $0.3Pd_{2.4}/CNT_5$ catalysts is shown in Fig. S35.† The observed evolution confirms the importance of this ratio to optimize the catalytic performances. The best compromise between high STY and high selectivity is obtained for the $0.6Pd_{2.4}/CNT_5$ catalyst. Considering that these catalysts were prepared from the same batch of $Pd_{2.4}$ particles and on the same CNT_5 support, it is difficult to rationalize the evolution of this ratio with the metal loading (Fig. S36†). It might be related to a higher degree of aggregation of $Pd_{2.4}$ particles on CNT_5 at low Pd loading, which will limit the spillover of the OAm ligands on the support and their further elimination upon washing.

Conclusions

Preformed palladium nanoparticles of different sizes bearing oleylamine as capping ligand were synthesized and immobilized on carbon nanotubes presenting different densities of oxygen functional groups. XPS and TPD analyses suggest that ligand spillover from the Pd particles to the support is more pronounced on the smaller Pd particles, which were the most active and selective for phenylacetylene hydrogenation. This study demonstrated that adjusting the surface functionalization of the carbon support can be a promising approach to control the capping ligand spillover and consequently the surface $Pd^{(0)}/Pd^{2+}$ and Pd/N ratio of small Pd particles (≈2.4 nm), which in turn can have a significant impact on the catalyst performances. Larger Pd particles (≈4.4 nm) are less subject to this spillover phenomenon and show lower catalytic performances. The use of Pd particles not stabilized by oleylamine allowed us to clarify the role of the amine ligand, which allows achieving a better selectivity to styrene. Finally, it appears that the Pd loading of the preformed nanoparticles is also an important parameter that must be considered. Indeed, the spatial distribution of the preformed particles must be impacted by the Pd loading, which also contributes to adjusting the surface $Pd^{(0)}/Pd^{2+}$ and Pd/N ratio and consequently the catalyst performances.

Data availability

The data that support the findings of the research are available on reasonable request from the corresponding author.

Author contributions

E. A. Leal Villarroel: investigation, formal analysis, original draft writing. C. Marcelot: investigation, formal analysis. C. C. Torres: project administration, funding acquisition, writing – review & editing. K. Soulantica: formal analysis, writing – review & editing. C. H. Campos: project administration, funding acquisition, writing – review & editing. P. Serp: project administration, funding acquisition, original draft writing, writing – review & editing.

Conflicts of interest

There are no conflicts of interest to declare.

Acknowledgements

This work was supported by ECOS Sud - ANID (project ECOS no. C21E03) and PROGRAMA DE COOPERACIÓN CIENTÍFICA ECOS-ANID 210036. Edgardo Leal thanks Grant ANID 242230083. The authors acknowledge Fondequip EQM160070 for TPD analysis.

Notes and references

1 T. W. van Deelen, C. Hernández Mejía and K. P. de Jong, *Nat. Catal.*, 2019, **2**, 955–970.
2 J. Liu, *ChemCatChem*, 2011, **3**, 934–948.
3 M. M. DeBusk, C. K. Narula and C. I. Contescu, *Surface Chemistry and Properties of Oxides as Catalyst Supports*, CRC Press, Boca Raton, FL, USA, United States, 2015.
4 J. Zhou, P. Yang, P. A. Kots, M. Cohen, Y. Chen, C. M. Quinn, M. D. de Mello, J. A. Boscoboinik, W. J. Shaw, S. Caratzoulas, W. Zheng and D. G. Vlachos, *Nat. Commun.*, 2023, **14**, 2293.
5 M. Jerigová, M. Odziomek and N. López-Salas, *ACS Omega*, 2022, **7**, 11544–11554.
6 I. C. Gerber and P. Serp, *Chem. Rev.*, 2020, **120**, 1250–1349.
7 T. Mitsui, M. K. Rose, E. Fomin, D. F. Ogletree and M. Salmeron, *Nature*, 2003, **422**, 705–707.
8 R. S. Oosthuizen and V. O. Nyamori, *Platinum Met. Rev.*, 2011, **55**, 154–169.
9 R. M. Mironenko, O. B. Belskaya and V. A. Likholobov, *Catal. Today*, 2020, **357**, 152–165.
10 S. Dong Jin, P. Tae-Jin and I. Son-Ki, *Carbon*, 1993, **31**, 427–435.
11 E. Castillejos, A. M. García-Minguillán, B. Bachiller-Baeza, I. Rodríguez-Ramos and A. Guerrero-Ruiz, *Catal. Today*, 2018, **301**, 248–257.
12 A. Cabiac, G. Delahay, R. Durand, P. Trens, B. Coq and D. Plée, *Carbon*, 2007, **45**, 3–10.
13 R. C. Contreras, B. Guicheret, B. F. Machado, C. Rivera-Cárcamo, M. A. Curiel Alvarez, B. Valdez Salas, M. Ruttert, T. Placke, A. Favre Réguillon, L. Vanoye, C. de Bellefon, R. Philippe and P. Serp, *J. Catal.*, 2019, **372**, 226–244.
14 L. Calvo, M. A. Gilarranz, J. A. Casas, A. F. Mohedano and J. J. Rodríguez, *Ind. Eng. Chem. Res.*, 2005, **44**, 6661–6667.
15 N. An, M. Zhang, Z. Zhang, Y. Dai, Y. Shen, C. Tang, X. Yuan and W. Zhou, *J. Colloid Interface Sci.*, 2018, **510**, 181–189.
16 P. Liu, W.-T. Chang, M.-Y. Wu, Y.-X. Li and J. Wang, *React. Kinet., Mech. Catal.*, 2015, **116**, 409–419.
17 X. Zhang, Q. Gu, Y. Ma, Q. Guan, R. Jin, H. Wang, B. Yang and J. Lu, *J. Catal.*, 2021, **400**, 173–183.
18 R. G. Rao, R. Blume, M. T. Greiner, P. Liu, T. W. Hansen, K. S. Dreyer, D. D. Hibbitts and J.-P. Tessonnier, *ACS Catal.*, 2022, **12**, 7344–7356.
19 J. Navarro-Ruiz, J. Audevard, M. Vidal, C. H. Campos, I. Del Rosal, P. Serp and I. C. Gerber, *ACS Catal.*, 2024, **14**, 7111–7126.
20 P. You, L. Wu, L. Zhou, Y. Xu and R. Qin, *Catalysts*, 2024, **14**, 545.
21 A. Lazzarini, A. Piovano, R. Pellegrini, G. Leofanti, G. Agostini, S. Rudić, M. R. Chierotti, R. Gobetto, A. Battiato, G. Spoto, A. Zecchina, C. Lamberti and E. Groppo, *Catal. Sci. Technol.*, 2016, **6**, 4910–4922.
22 M. Stucchi, S. Capelli, A. Villa, B. D. Vandegehuchte and L. Prati, *ChemCatChem*, 2024, **16**, e202301639.

23 S. Domínguez-Domínguez, Á. Berenguer-Murcia, B. K. Pradhan, Á. Linares-Solano and D. Cazorla-Amorós, *J. Phys. Chem. C*, 2008, **112**, 3827–3834.
24 R. Sato, M. Kanehara and T. Teranishi, *Small*, 2011, **7**, 469–473.
25 B. Kılıç, S. Şencanlı and Ö. Metin, *J. Mol. Catal. A: Chem.*, 2012, **361–362**, 104–110.
26 L. Vanoye, B. Guicheret, C. Rivera-Cárcamo, J. Audevard, J. Navarro-Ruiz, I. del Rosal, I. C. Gerber, C. H. Campos, B. F. Machado, J. Volkman, R. Philippe, P. Serp and A. Favre-Réguillon, *J. Catal.*, 2023, **424**, 173–188.
27 A. Borodziński and M. Bonarowska, *Langmuir*, 1997, **13**, 5613–5620.
28 I. Gerber, M. Oubenali, R. Bacsa, J. Durand, A. Gonçalves, M. F. R. Pereira, F. Jolibois, L. Perrin, R. Poteau and P. Serp, *Chem. – Eur. J.*, 2011, **17**, 11467–11477.
29 V. Datsyuk, M. Kalyva, K. Papagelis, J. Parthenios, D. Tasis, A. Siokou, I. Kallitsis and C. Galiotis, *Carbon*, 2008, **46**, 833–840.
30 J. P. Olivier and M. Winter, *J. Power Sources*, 2001, **97–98**, 151–155.
31 S. Kundu, Y. Wang, W. Xia and M. Muhler, *J. Phys. Chem. C*, 2008, **112**, 16869–16878.
32 Z. R. Yue, W. Jiang, L. Wang, S. D. Gardner and C. U. Pittman, *Carbon*, 1999, **37**, 1785–1796.
33 M. Smith, L. Scudiero, J. Espinal, J.-S. McEwen and M. Garcia-Perez, *Carbon*, 2016, **110**, 155–171.
34 J.-H. Zhou, Z.-J. Sui, J. Zhu, P. Li, D. Chen, Y.-C. Dai and W.-K. Yuan, *Carbon*, 2007, **45**, 785–796.
35 N. Fairley, G. Compagnini, V. Scardaci, J. Baltrus, A. Roberts, A. Barlow, P. Cumpson and J. Baltrusaitis, *Surf. Interface Anal.*, 2023, **55**, 165–175.
36 J. L. Figueiredo, M. F. R. Pereira, M. M. A. Freitas and J. J. M. Órfão, *Ind. Eng. Chem. Res.*, 2007, **46**, 4110–4115.
37 R. P. Rocha, M. F. R. Pereira and J. L. Figueiredo, *Catal. Today*, 2023, **418**, 114136.
38 K. Murakami, R. Kondo, K. Fuda and T. Matsunaga, *J. Colloid Interface Sci.*, 2003, **260**, 176–183.
39 V. Mazumder and S. Sun, *J. Am. Chem. Soc.*, 2009, **131**, 4588–4589.
40 R. Sato, M. Kanehara and T. Teranishi, *Small*, 2011, **7**, 469–473.
41 H. Guo, Y. Chen, M. B. Cortie, X. Liu, Q. Xie, X. Wang and D.-L. Peng, *J. Phys. Chem. C*, 2014, **118**, 9801–9808.
42 Z. Fereshteh, M. Salavati-Niasari, K. Saberyan, S. M. Hosseinpour-Mashkani and F. Tavakoli, *J. Cluster Sci.*, 2012, **23**, 577–583.
43 Z. Wang, C. Jiang, R. Huang, H. Peng and X. Tang, *J. Phys. Chem. C*, 2014, **118**, 1155–1160.
44 S. Mourdikoudis and L. M. Liz-Marzán, *Chem. Mater.*, 2013, **25**, 1465–1476.
45 H. Lu, W. Tang, X. Liu, B. Wang and Z. Huang, *J. Mater. Sci.*, 2017, **52**, 4483–4492.
46 Y.-H. Kim, Y. Zhai, E. A. Gaulding, S. N. Habisreutinger, T. Moot, B. A. Rosales, H. Lu, A. Hazarika, R. Brunecky, L. M. Wheeler, J. J. Berry, M. C. Beard and J. M. Luther, *ACS Nano*, 2020, **14**, 8816–8825.
47 E. Xiu-Tian-Feng, Y. Zhang, J.-J. Zou, L. Wang and X. Zhang, *Ind. Eng. Chem. Res.*, 2014, **53**, 12312–12318.
48 A. M. Karim, N. Al Hasan, S. Ivanov, S. Siefert, R. T. Kelly, N. G. Hallfors, A. Benavidez, L. Kovarik, A. Jenkins, R. E. Winans and A. K. Datye, *J. Phys. Chem. C*, 2015, **119**, 13257–13267.
49 J.-H. Liu, C.-Q. Lv, Y. Guo and G.-C. Wang, *Appl. Surf. Sci.*, 2013, **271**, 291–298.
50 M. Brun, A. Berthet and J. C. Bertolini, *J. Electron Spectrosc. Relat. Phenom.*, 1999, **104**, 55–60.
51 Y. Shi, S. Yin, Y. Ma, D. Lu, Y. Chen, Y. Tang and T. Lu, *J. Power Sources*, 2014, **246**, 356–360.
52 K. Kaźmierczak, D. Yi, A. Jaud, P.-F. Fazzini, M. Estrader, G. Viau, P. Decorse, J.-Y. Piquemal, C. Michel, M. Besson, K. Soulantica and N. Perret, *J. Phys. Chem. C*, 2021, **125**, 7711–7720.
53 J. Liu, J. Hao, C. Hu, B. He, J. Xi, J. Xiao, S. Wang and Z. Bai, *J. Phys. Chem. C*, 2018, **122**, 2696–2703.
54 E. Ramirez, S. Jansat, K. Philippot, P. Lecante, M. Gomez, A. M. Masdeu-Bultó and B. Chaudret, *J. Organomet. Chem.*, 2004, **689**, 4601–4610.
55 B. Cornelio, G. A. Rance, M. Laronze-Cochard, A. Fontana, J. Sapi and A. N. Khlobystov, *J. Mater. Chem. A*, 2013, **1**, 8737–8744.
56 T. Ramanathan, F. T. Fisher, R. S. Ruoff and L. C. Brinson, *Chem. Mater.*, 2005, **17**, 1290–1295.
57 A. B. Dongil, B. Bachiller-Baeza, A. Guerrero-Ruiz, I. Rodríguez-Ramos, A. Martínez-Alonso and J. M. D. Tascón, *J. Colloid Interface Sci.*, 2011, **355**, 179–189.
58 H. F. Gorgulho, J. P. Mesquita, F. Gonçalves, M. F. R. Pereira and J. L. Figueiredo, *Carbon*, 2008, **46**, 1544–1555.
59 X. Wang, P. Sonström, D. Arndt, J. Stöver, V. Zielasek, H. Borchert, K. Thiel, K. Al-Shamery and M. Bäumer, *J. Catal.*, 2011, **278**, 143–152.
60 B. Jürgens, H. Borchert, K. Ahrenstorf, P. Sonström, A. Pretorius, M. Schowalter, K. Gries, V. Zielasek, A. Rosenauer, H. Weller and M. Bäumer, *Angew. Chem., Int. Ed.*, 2008, **47**, 8946–8949.
61 B. Donoeva and P. E. de Jongh, *ChemCatChem*, 2018, **10**, 989–997.
62 R. G. Rao, R. Blume, T. W. Hansen, E. Fuentes, K. Dreyer, S. Moldovan, O. Ersen, D. D. Hibbitts, Y. J. Chabal, R. Schlögl and J.-P. Tessonnier, *Nat. Commun.*, 2017, **8**, 340.
63 G. Collins, F. Davitt, C. O'Dwyer and J. D. Holmes, *ACS Appl. Nano Mater.*, 2018, **1**, 7129–7138.
64 T. T. Nguyen and P. Serp, *ChemCatChem*, 2013, **5**, 3595–3603.
65 M. W. Marshall, S. Popa-Nita and J. G. Shapter, *Carbon*, 2006, **44**, 1137–1141.
66 R. Benbalagh, F. Rochet, A. Moisset, A. Sodreau, C. Bories, C. Salzemann, C. Petit and M. Petit, *J. Phys. Chem. C*, 2024, **128**, 3408–3422.
67 D. Wilson and M. A. Langell, *Appl. Surf. Sci.*, 2014, **303**, 6–13.
68 D. Yi, C. Marcelot, I. Romana, M. Tassé, P.-F. Fazzini, L. Peres, N. Ratel-Ramond, P. Decorse, B. Warot-Fonrose, G.

Viau, P. Serp and K. Soulantica, *Nanoscale*, 2023, **15**, 1739–1753.
69 Á. Arnosa-Prieto, M. A. González-Gómez, P. García-Acevedo, L. de Castro-Alves, Y. Piñeiro and J. Rivas, *Mater. Today Chem.*, 2024, **35**, 101854.
70 I. A. Safo, C. Dosche and M. Özaslan, *ChemPhysChem*, 2019, **20**, 3010–3023.
71 R. J. J. Jansen and H. van Bekkum, *Carbon*, 1995, **33**, 1021–1027.
72 J. P. Gallivan and D. A. Dougherty, *J. Am. Chem. Soc.*, 2000, **122**, 870–874.
73 B. F. Machado, M. Oubenali, M. Rosa Axet, T. T. Nguyen, M. Tunckol, M. Girleanu, O. Ersen, I. C. Gerber and P. Serp, *J. Catal.*, 2014, **309**, 185–198.
74 S. Kundu, W. Xia, W. Busser, M. Becker, D. A. Schmidt, M. Havenith and M. Muhler, *Phys. Chem. Chem. Phys.*, 2010, **12**, 4351–4359.
75 K. F. Ortega, R. Arrigo, B. Frank, R. Schlögl and A. Trunschke, *Chem. Mater.*, 2016, **28**, 6826–6839.
76 L.-P. Xu, S. Qian, Z. Zhuang, J.-Q. Yu and D. G. Musaev, *Nat. Commun.*, 2022, **13**, 315.
77 F. Lan, J. Bai and H. Wang, *RSC Adv.*, 2018, **8**, 16866–16872.
78 K. Chang, C. Podder and H. Pan, *ACS Appl. Nano Mater.*, 2023, **6**, 23418–23429.
79 D. E. Gardin and G. A. Somorjai, *J. Phys. Chem.*, 1992, **96**, 9424–9431.
80 P. A. Attwood, B. D. McNicol, R. T. Short and J. A. van Amstel, *J. Chem. Soc., Faraday Trans. 1*, 1980, **76**, 2310–2321.
81 X. Song, F. Shao, Z. Zhao, X. Li, Z. Wei and J. Wang, *Chem. Eng. Sci.*, 2023, **274**, 118609.
82 S. Capelli, S. Cattaneo, M. Stucchi, B. D. Vandegehuchte, A. Chieregato, A. Villa and L. Prati, *Catalysts*, 2022, **12**, 251.
83 L. He, Y. Wang, C. Wang, Z. Liu and Z. Xie, *Front. Chem.*, 2022, 10.
84 S. G. Kwon, G. Krylova, A. Sumer, M. M. Schwartz, E. E. Bunel, C. L. Marshall, S. Chattopadhyay, B. Lee, J. Jellinek and E. V. Shevchenko, *Nano Lett.*, 2012, **12**, 5382–5388.
85 H. A. Al-Wadhaf, V. M. Karpov and E. A. Katsman, *Catal. Commun.*, 2018, **116**, 67–71.
86 S. Wang, T. Liu, Y. Zhu, X. Liu, Q. Luo, M. Zhu, T. Ding and T. Yao, *J. Phys. Chem. C*, 2023, **127**, 5911–5919.
87 J. Audevard, J. Navarro-Ruiz, V. Bernardin, Y. Tison, A. Corrias, I. Del Rosal, A. Favre-Réguillon, R. Philippe, I. C. Gerber and P. Serp, *ChemCatChem*, 2023, **15**, e202300036.
88 A. Garcia-Ortiz, J. D. Vidal, S. Iborra, M. J. Climent, J. Cored, D. Ruano, V. Pérez-Dieste, P. Concepción and A. Corma, *J. Catal.*, 2020, **389**, 706–713.
89 S. Wang, Z. Xin, X. Huang, W. Yu, S. Niu and L. Shao, *Phys. Chem. Chem. Phys.*, 2017, **19**, 6164–6168.
90 W. Wu, W. Zhang, Y. Long, J. Qin, H. Wen and J. Ma, *J. Colloid Interface Sci.*, 2018, **531**, 642–653.
91 W. Zhang, W. Wu, Y. Long, J. Qin, F. Wang and J. Ma, *ChemCatChem*, 2019, **11**, 1510–1517.
92 L. Ma, P. Jiang, K. Wang, K. Lan, X. Huang, M. Yang, L. Gong, Q. Jia, X. Mu, Y. Xiong and R. Li, *J. Alloys Compd.*, 2021, **868**, 159047.
93 W. Zhang, F. Wang, X. Li, Y. Liu, Y. Liu and J. Ma, *Appl. Surf. Sci.*, 2017, **404**, 398–408.
94 W. Yu, Z. Xin, S. Niu, T.-W. Lin, W. Guo, Y. Xie, Y. Wu, X. Ji and L. Shao, *Catal. Sci. Technol.*, 2017, **7**, 4934–4939.
95 G. Carturan, G. Facchin, G. Cocco, S. Enzo and G. Navazio, *J. Catal.*, 1982, **76**, 405–417.
96 Y. Wu, X. Lu, P. Cui, W. Jia, J. Zhou, Y. Wang, H. Zahid, Y. Wu, M. U. Rafique, X. Yin, B. Li, L. Wang and G. Xiang, *Nano Res.*, 2024, **17**, 3707–3713.
97 C. Li, Z. Shao, M. Pang, C. T. Williams and C. Liang, *Catal. Today*, 2012, **186**, 69–75.
98 A. Mollar-Cuni, D. Ventura-Espinosa, S. Martín, Á. Mayoral, P. Borja and J. A. Mata, *ACS Omega*, 2018, **3**, 15217–15228.
99 J. G. Smith and P. K. Jain, *J. Am. Chem. Soc.*, 2016, **138**, 6765–6773.
100 Z. Xia, S. Zhang, F. Liu, Y. Ma, Y. Qu and C. Wu, *J. Phys. Chem. C*, 2019, **123**, 2182–2188.
101 K. Choe, F. Zheng, H. Wang, Y. Yuan, W. Zhao, G. Xue, X. Qiu, M. Ri, X. Shi, Y. Wang, G. Li and Z. Tang, *Angew. Chem., Int. Ed.*, 2020, **59**, 3650–3657.
102 A. Boretskaya, I. Il'yasov, A. Popov and A. Lamberov, *Mater. Today Chem.*, 2021, **19**, 100387.
103 V. A. Vons, H. Leegwater, W. J. Legerstee, S. W. H. Eijt and A. Schmidt-Ott, *Int. J. Hydrogen Energy*, 2010, **35**, 5479–5489.
104 X. Sun, P. Ariza, M. Ortiz and K. G. Wang, *Int. J. Hydrogen Energy*, 2018, **43**, 5657–5667.
105 J. Yang, J. Y. Lee and H.-P. Too, *Anal. Chim. Acta*, 2006, **571**, 206–210.
106 J. K. Edwards, J. Pritchard, M. Piccinini, G. Shaw, Q. He, A. F. Carley, C. J. Kiely and G. J. Hutchings, *J. Catal.*, 2012, **292**, 227–238.
107 Z. Liu, H. Yang, F. Wang, Y. Lv, L. Zhou, Y. Xie and H. Wang, *Fuel*, 2024, **366**, 131389.
108 V. Z. Radkevich, T. L. Senko, K. Wilson, L. M. Grishenko, A. N. Zaderko and V. Y. Diyuk, *Appl. Catal., A*, 2008, **335**, 241–251.
109 B. Gong, A. Ikematsu and K. Waki, *Carbon*, 2017, **114**, 526–532.
110 S.-Y. Wu and J.-J. Ho, *J. Phys. Chem. C*, 2014, **118**, 26764–26771.
111 X. Deng, D. Alfonso, T.-D. Nguyen-Phan and D. R. Kauffman, *ACS Catal.*, 2023, **13**, 15301–15309.
112 Z. Bao, H. Zhou, X. Song, Y. Gao, G. Zhuang, S. Deng, Z. Wei, X. Zhong and J. Wang, *ChemCatChem*, 2019, **11**, 1278–1285.
113 Q.-Q. Yan, D.-X. Wu, S.-Q. Chu, Z.-Q. Chen, Y. Lin, M.-X. Chen, J. Zhang, X.-J. Wu and H.-W. Liang, *Nat. Commun.*, 2019, **10**, 4977.
114 M. Guo, C. Li and Q. Yang, *Catal. Sci. Technol.*, 2017, **7**, 2221–2227.
115 M. Qiao, Y. Wang, S. Gao, Q. Fu, X. Wang, R. Qin and N. Zheng, *ACS Catal.*, 2024, **14**, 11468–11476.
116 M. Gurrath, T. Kuretzky, H. P. Boehm, L. B. Okhlopkova, A. S. Lisitsyn and V. A. Likholobov, *Carbon*, 2000, **38**, 1241–1255.
117 Z. Wang, B. Zhang, S. Yang, X. Yang, F. Meng, L. Zhai, Z. Li, S. Zhao, G. Zhang and Y. Qin, *J. Catal.*, 2022, **414**, 385–393.

118 C. Rivera-Cárcamo, I. C. Gerber, I. del Rosal, B. Guicheret, R. Castro Contreras, L. Vanoye, A. Favre-Réguillon, B. F. Machado, J. Audevard, C. de Bellefon, R. Philippe and P. Serp, *Catal. Sci. Technol.*, 2021, **11**, 984–999.

119 Q. Wang, Z. Li, Y. Zhou, Y. Wen, J. Zhai, L. Xu, Q. Zhang, Y. Qin, C. Lu, Q. Zhang and X. Li, *Ind. Eng. Chem. Res.*, 2024, **63**, 15778–15789.

120 A. Holm, E. D. Goodman, J. H. Stenlid, A. Aitbekova, R. Zelaya, B. T. Diroll, A. C. Johnston-Peck, K.-C. Kao, C. W. Frank, L. G. M. Pettersson and M. Cargnello, *J. Am. Chem. Soc.*, 2020, **142**, 14481–14494.

121 K. R. G. Lim, S. K. Kaiser, H. Wu, S. Garg, C. R. O'Connor, C. Reece, M. Aizenberg and J. Aizenberg, *ACS Nano*, 2024, **18**, 15958–15969.

122 K. R. G. Lim, S. K. Kaiser, H. Wu, S. Garg, M. Perxés Perich, J. E. S. van der Hoeven, M. Aizenberg and J. Aizenberg, *Nat. Catal.*, 2024, **7**, 172–184.